OPEN ACCESS

Sensitive and Sustainable Voltammetric Determination of Gilteritinib Using a SnO_2/Co_3O_4-Modified Carbon Paste Electrode Supported by DFT Analysis

To cite this article: Çiğdem Aybüke Özata *et al* 2026 *ECS Sens. Plus* **5** 033604

View the article online for updates and enhancements.

You may also like

- A Facile Electrochemical Sensor Based on NiO-ZnO/MWCNT-COOH Modified GCE for Simultaneous Quantification of Imatinib and Itraconazole
Haicheng Chen, Kang Luo and Kang Li
- A Sensitive Electrochemical DNA Biosensor for Determination of Anti-Cancer Drug Gemcitabine Based on an AuNPs/MWCNTs/Carbon Paste Electrode
Masoumeh Mohammadi, Amir Abbas Rafati and Ahmad Bagheri
- A robust electrochemical sensing platform for the detection of erlotinib based on nitrogen-doped graphene quantum dots/copper nanoparticles-polyaniline-graphene oxide nanohybrid
Hamidreza Rahmanian, Zarrin Es'haghi and Mehdi Dadmehr

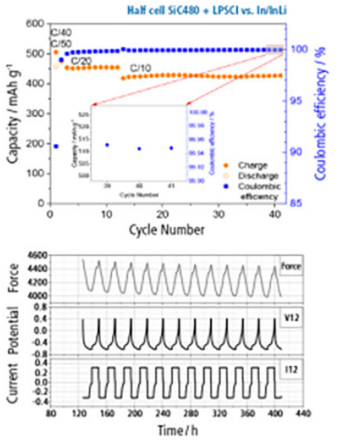
The New PAT-Cell-Solid!

EL-CELL® electrochemical test equipment

Cycle Solid-State Batteries Under Controlled Pressure of up to 300 MPa (6 mm Diameter)!



- Adjust and measure a force of up to 9000 N on the cell stack!
Force adjustment possible throughout the entire experiment
- Built-in force, and temperature sensors!
With optional gas pressure sensor and gas in- and outlet
- PAT-Solid-Core for easy assembly and reproducible results!
Press and cycle solid-state batteries with 6 or 10 mm electrode diameter
- Cableless and highly sealed battery test cell!
For precise long-term measurements of solid-state cell chemistries



Learn more on our product website: Scan me!

Download the data sheet (PDF): Scan me!

Or contact us directly:

+49 40 79012-734

sales@el-cell.com

www.el-cell.com

This content was downloaded from IP address 80.251.45.167 on 17/08/2026 at 22:20

ECS Sensors Plus, 2026 **5** 033604

Sensitive and Sustainable Voltammetric Determination of Gilteritinib Using a SnO_2/Co_3O_4-Modified Carbon Paste Electrode Supported by DFT Analysis

Çiğdem Aybüke Özata,[1,2,z] Nevin Erk,[1,z] Celal Tuğrul Zeyrek,[3] Furkan Uzcan,[4] and Mustafa Soylak,[4,5,6]

[1]*Faculty of Pharmacy Department of Analytical Chemistry, Ankara University, 06560 Ankara, Turkey*
[2]*The Graduate School of the Health Sciences, Ankara University, 06110 Ankara, Turkey*
[3]*Ankara University, Institute of Nuclear Sciences, Ankara 06100, Turkey*
[4]*Faculty of Sciences, Department of Chemistry, Erciyes University, 38039 Kayseri, Turkey*
[5]*Technology Research & Application Center (TAUM), Erciyes University, 38039 Kayseri, Turkey*
[6]*Turkish Academy of Sciences (TUBA), Ankara, Turkey*

An electrochemical sensor based on a SnO_2/Co_3O_4-modified carbon paste electrode (CPE) was developed for the quantitative determination of gilteritinib (GIL), a drug used in the treatment of acute myeloid leukemia. The SnO_2/Co_3O_4 nanocomposite was synthesized via a precipitation–calcination route and characterized by XRD, FTIR, FE-SEM, and STEM analyses. The electrochemical properties of the modified electrode were investigated using cyclic voltammetry (CV) and electrochemical impedance spectroscopy (EIS). Compared with bare CPE, the SnO_2/Co_3O_4/CPE exhibited enhanced electrocatalytic activity and faster electron-transfer kinetics, evidenced by lower peak separation ($\Delta E_p = 0.19$ V), higher peak current ($I_p = 35$ μA), and reduced charge-transfer resistance ($R_{ct} = 2590$ Ω). Quantitative determination of GIL was carried out using differential pulse voltammetry (DPV), yielding a wide linear range of 0.00031–11.640 μM with limits of detection and quantification of 0.093 and 0.309 nM, respectively. The sensor showed excellent repeatability (RSD = 1.1%), reproducibility (RSD = 0.5%), high sensitivity (13.17 μA μM^{-1} cm^{-2}), and good selectivity, with recoveries between 96.9% and 103.5%. Greenness assessment using AGREE, GAPI, and BAGI confirmed the environmentally friendly nature of the method. Overall, the proposed platform provides a sensitive and reliable approach for GIL determination with potential application in therapeutic monitoring.
© 2026 The Author(s). Published on behalf of The Electrochemical Society by IOP Publishing Limited. This is an open access article distributed under the terms of the Creative Commons Attribution 4.0 License (CC BY, https://creativecommons.org/licenses/by/4.0/), which permits unrestricted reuse of the work in any medium, provided the original work is properly cited.
[DOI: 10.1149/2754-2726/ae90bd]

Manuscript submitted June 26, 2026; revised manuscript received July 21, 2026. Published August 6, 2026.

Supplementary material for this article is available online

Acute myeloid leukemia (AML) is a hematological malignancy characterized by the uncontrolled proliferation of immature myeloid cells in the bone marrow, which disrupts normal hematopoiesis and leads to severe infections, anemia, and an increased risk of hemorrhage.[1–3] Among the therapeutic strategies developed for AML, targeted kinase inhibitors have gained considerable attention. Gilteritinib (GIL) is an orally active small-molecule inhibitor that targets the AXL receptor tyrosine kinase and the FMS-like tyrosine kinase 3 (FLT3) signaling pathway, both of which play crucial roles in leukemic cell survival and proliferation.[4–6] Due to its clinical efficacy, GIL has been approved in several regions, including the United States, the European Union, Japan, and Canada, for the treatment of adults with relapsed or refractory AML.[7,8]

Despite its therapeutic benefits, the safe use of GIL requires careful monitoring due to potential adverse effects and drug–drug interactions. GIL is primarily metabolized by the cytochrome P450 enzyme CYP3A4, and co-administration with strong CYP3A4 inhibitors can significantly increase systemic exposure, potentially leading to severe toxicities.[9,10] Therefore, pharmacokinetic evaluation and therapeutic drug monitoring, dependable analytical approaches are required for the determination of GIL in pharmaceutical products and biological matrices.

Despite the clinical significance of GIL, the current analytical landscape for its determination is notably sparse, particularly concerning rapid and cost-effective monitoring. While various chromatographic and mass spectrometric techniques, including HPLC,[11] UPLC-MS/MS,[12] LC–MS/MS,[13] and UHPLC-PDA,[14] have been applied to the analysis of anticancer agents, their widespread implementation is frequently hindered by prohibitively expensive instrumentation, arduous sample pretreatment protocols, and substantial solvent consumption. Consequently, the exploration of novel nanostructured materials is essential to overcome the limitations of existing methods and provide a more accessible, sustainable, and sensitive analytical tool for clinical oncology. To date, only a single electrochemical method for the determination of GIL has been reported, which was previously introduced by our group using a nanocomposite-modified glassy carbon electrode.[15]

The performance of an electrode system in electrooxidation largely depends on the materials chosen for electrode modification. These materials should ideally exhibit a large surface area, suitable pore architecture, excellent electrical conductivity that promotes electron transfer, and strong electrochemical stability during operation.[16] Thanks to advances in nanotechnology, sensors utilizing micro-and nanomaterials have shown significant improvements in analytical capabilities, such as enhanced sensitivity, wider linear range, lower detection limits, faster response times, and better stability, selectivity, and reproducibility. Among these innovative materials, carbon nanostructures and metal-based nanocomposites have consistently contributed to the progress of electrochemical sensing systems.[17]

SnO_2 and Co_3O_4 each provide distinct electrochemical advantages that are particularly relevant for the oxidation of GIL. SnO_2, a wide-bandgap n-type semiconductor, contributes high chemical stability, enhanced surface area, and fast electron mobility, enabling stable and conductive sensing surfaces.[18,19] Co_3O_4, a p-type semiconductor, offers rich redox chemistry (Co^{2+}/Co^{3+} and Co^{3+}/Co^{4+} transitions) that promotes catalytic oxidation processes.[18,20] When combined in a SnO_2/Co_3O_4 nanocomposite, the interface naturally forms a p–n heterojunction that facilitates accelerated charge separation and reduces charge-transfer resistance, resulting in faster interfacial electron transfer.[18,19] Unlike single metal oxides, which

[z] E-mail: caozata@ankara.edu.tr; erk@pharmacy.ankara.edu.tr

typically provide either high conductivity (e.g. SnO_2) or strong electrocatalytic activity (e.g. Co_3O_4), the composite integrates both features simultaneously. Therefore, SnO_2/Co_3O_4-modified CPE benefits from the combined strengths of both oxides, leading to a more efficient and robust electrochemical sensing platform. Such a combination is particularly advantageous for GIL, whose diffusion-controlled electro-oxidation requires fast charge-transfer kinetics and a highly conductive sensing interface. As a result, the SnO_2/Co_3O_4 nanocomposite provides improved sensitivity, selectivity, and signal stability compared to single-oxide modifiers.[18,20,21] Crucially, while single-oxide modifiers or traditional solid-state electrodes face operational constraints such as surface fouling and time-consuming polishing, the integration of this p–n heterojunction nanocomposite into a carbon paste matrix provides a distinct novelty. The resulting SnO_2/Co_3O_4 platform synergizes accelerated interfacial charge-transfer kinetics with a rapidly renewable sensing surface, overcoming the key limitations of previously reported sensors and enabling lower detection limits and broader linear dynamic range for GIL quantification.[15]

Carbon-based electrodes are widely used in electrochemical sensing due to their wide potential window, high conductivity, and chemical stability.[22–24] Among them, carbon paste electrodes (CPEs) are particularly attractive because of their low cost, simple preparation, and easy surface renewal. Unlike glassy carbon electrodes, which require time-consuming polishing procedures and are susceptible to surface fouling, the surface of a CPE can be rapidly renewed by simple mechanical replacement of the paste, providing a fresh and reproducible sensing interface.[25] These features make CPEs suitable platforms for the development of practical and sustainable electrochemical sensors.[26–28] These features ultimately underpinned our choice of CPE as the optimal platform for the sensitive voltammetric detection of GIL.

Computational chemistry methods such as DFT and MD have been widely employed to investigate the structural, electronic, and interactional properties of bioactive molecules. DFT calculations provide valuable insights into the stability, reactivity, and frontier molecular orbitals of drug candidates, while MD enables the prediction of non-covalent interactions between ligands and specific biological targets[29–31] Quantum mechanical calculations for GIL were performed at B3LYP/6–31 + G (d, p) level by using DFT. The total energy, chemical parameters, the highest occupied (HOMO) and lowest unoccupied (LUMO) molecular orbital energies and configrations and molecular electrostatic potential (MEP) surfaces of GIL were predicted by DFT. On the other hand, the MD studies of GIL with AXL receptor tyrosine kinase and FMS-like tyrosine kinase 3 (FLT3) receptor have been reported by Elasbali et al.[32] and Das et al.[33] very recently. As mentioned above, concomitant use of GIL with a strong or moderate CYP3A4 inhibitor is generally contraindicated, and alternative treatment options are recommended to reduce drug–drug interactions. Accordingly, MD analyses were performed to examine the binding behavior of GIL with CYP3A4 inhibitors and to elucidate the non-covalent interactions of the optimized GIL molecule within the active region of the cytochrome P450 enzyme (CYP3A4, PDB ID: 1TQN). Therefore, our MD results may also guide the investigation of factors that may negatively affect drug therapy based on inhibition of CYP3A4 activities of GIL.

In this study, a SnO_2/Co_3O_4 nanocomposite-modified carbon paste electrode (SnO_2/Co_3O_4/CPE) was developed for the sensitive voltammetric determination of GIL. Compared with our previously reported glassy carbon electrode system, the proposed platform offers the advantages of a renewable electrode surface and improved analytical performance. DFT calculations were performed to investigate the electronic properties and electrochemical reactivity of GIL, while molecular docking studies were conducted to explore its interaction with the CYP3A4 enzyme, which plays a key role in its metabolic pathway. The developed sensor was successfully applied for the determination of GIL in pharmaceutical and biological samples, demonstrating its potential as a simple, sensitive, and cost-effective analytical platform.

Methodology

Chemicals and reagents.—Details of the chemicals and reagents used are provided in the Supporting Information.

Instruments.—Details of the instruments used are provided in the Supporting Information.

Synthesis of SnO_2/Co_3O_4 nanoflowers.—The standard synthesis procedure commenced with the dissolution of 1 mmol tin(IV) chloride pentahydrate and 10 mmol sodium hydroxide in separate portions of distilled water (100 ml and 5 ml, respectively). These solutions were then thoroughly mixed to form a clear solution. Subsequently, this transparent solution was combined with 1 mmol cobalt(II) nitrate hexahydrate, previously dissolved in 50 ml of distilled water and stirred continuously using a magnetic stirrer. After two hours of stirring, a pink suspension was obtained and left to stand at ambient temperature overnight. The resulting $CoSn(OH)_6$ precursor was then isolated via centrifugation, thoroughly washed, and dried. To obtain the target composite material (SnO_2/Co_3O_4 nanoflowers), the dried precursor was subjected to calcination at 700 °C for three hours in a muffle furnace. During this thermal treatment, $CoSn(OH)_6$ underwent dehydration followed by gradual conversion into mixed tin and cobalt oxides, accompanied by phase separation. Upon completion of this transformation, the initial pink $CoSn(OH)_6$ precursor was fully converted into black, porous SnO_2/Co_3O_4 nanoflowers.[34]

Fabrication of the SnO_2/Co_3O_4 modified CPE.—To prepare the SnO_2/Co_3O_4-modified carbon paste electrode (SnO_2/Co_3O_4/CPE), 0.9 g of graphite powder was thoroughly mixed with 0.1 g of SnO_2/Co_3O_4 using a porcelain mortar and pestle to ensure homogeneity. The mixture was then moistened with a small amount of diethyl ether and blended with paraffin oil, which served as the binding agent, until a uniformly textured carbon paste was formed. This paste was packed into the electrode cavity, and the surface was smoothed by removing any excess material to obtain a clean, consistent interface. For comparison, an unmodified CPE was prepared following the same procedure, excluding the SnO_2/Co_3O_4 component, to maintain consistency between the reference and modified electrodes.

Processing of spiked samples for GIL quantification.—The applicability of the fabricated electrode was demonstrated through the determination of GIL in various real samples. Spiked biological and pharmaceutical samples were prepared using a procedure adapted from our previous work.[35]

Computational studies.—The total energy, frontier molecular orbital energies and MEP surfaces of GIL were determined at same level of DFT theory. The chemical parameters were predicted by utilzing the Koopman's theorem.[36,37] The MD studies were impelmented to elucidate the interaction behavior between optimized molecule of GIL and the catalytic pocket of the cytochrome P450 enzyme CYP3A4 (PDB ID: 1TQN). The crystal structure of the cytochrome P450 enzyme CYP3A4 was obtained from web site of PDB (www.rcsb.org/pdb). The water, solvent molecules and ions were omitted in the crystal structure of the cytochrome P450 enzyme CYP3A4. The heme molecule was not removed in the structure of the cytochrome P450 enzyme CYP3A4 to reveal interactions between optimized molecule GIL and heme molecule of the cytochrome P450 enzyme CYP3A4 (PDB ID: 1TQN). During the MD studies, a grid box with dimensions of 30 × 30 × 30 Å was defined to cover

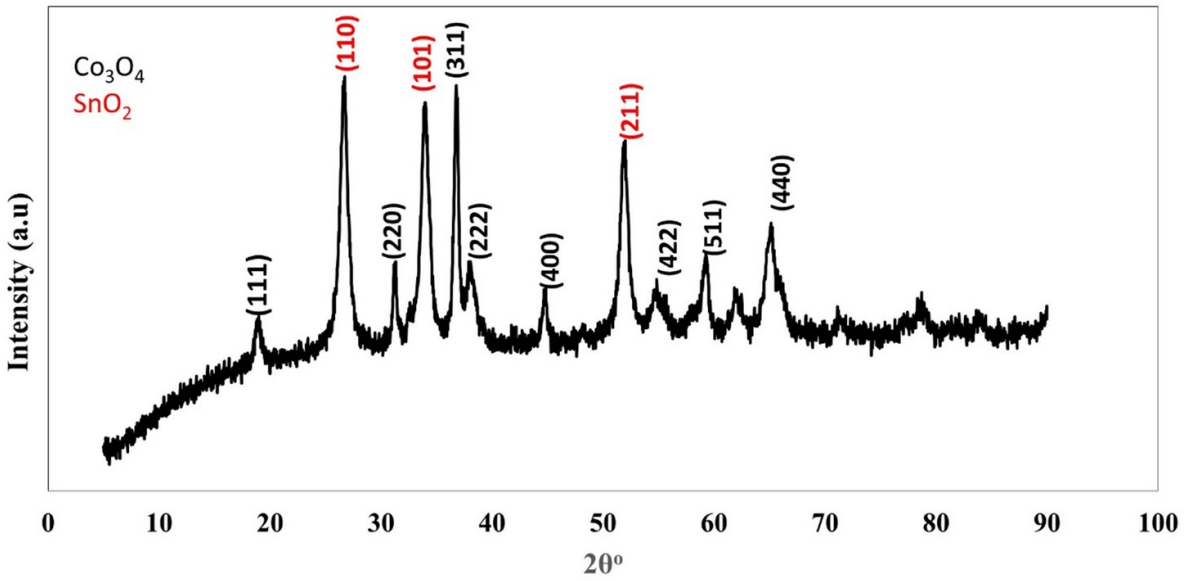


Figure 1. XRD pattern of SnO_2/Co_3O_4 nanoflowers. The diffraction peaks are indexed to SnO_2 (JCPDS 01-072-1147) and Co_3O_4 (JCPDS 00-043-1003), confirming the coexistence of both crystalline phases without the formation of new phases.

the active site region of the enzyme, centered at $x = -19.128$, $y = -23.978$, and $z = -13.910$, while the conformation exhibiting the lowest binding free energy (ΔG) was considered the most favorable docking pose.[38]

Results and Discussion

Characterization of SnO_2/Co_3O_4 nanoflowers.—*Fourier-transform infrared spectroscopy (FTIR) analysis.*—The synthesized SnO_2/Co_3O_4 nanoflowers were characterized by XRD, FT-IR, FE-SEM and STEM methods. The FT-IR spectra of SnO_2/Co_3O_4 nanoflowers is displayed in figure S1. The wide vibration bands detected at 557 and 654 cm^{-1} could be associated with the stretching vibration of metal–oxygen (Co–O or Sn–O). The vibrational bands can be attributed to O–H stretching (about 2972 cm^{-1}) and O–H bending vibration (approximately 1658 cm^{-1}). Because of nanoflowers high surface-to-volume ratio, water is often absorbed from the environment and visible in the absorption bands between 1658 and 2972 cm^{-1}.[39,40]

X-ray diffraction analysis.—The crystal structure of the SnO_2–Co_3O_4 nanoflowers is confirmed by the XRD patterns displayed in Fig. 1, which are in good accordance with the JCPD cards 00-043-1003 and 01-072-1147, respectively. The (111), (220), (311), (222), (400), (422), (511), and (440) planes of cubic Co_3O_4 are represented by the diffraction peaks at 19.0, 31.2, 36.8, 38.5, 44.8, 55.7, 59.3, and 65.3° of 2θ values. (JCPD card no: 00-043-1033). According to JCPDS card no. 01-072-1147, SnO_2 is effectively composited with Co_3O_4, as evidenced by SnO_2 peaks seen at 2θ values of 26.4, 33.8, and 51.8°, which correspond to the (110), (101), and (211) planes. All diffraction peaks were indexed to SnO_2 (JCPDS 01-072-1147) and Co_3O_4 (JCPDS 00-043-1003). The composite pattern matches well with the reference data of pure SnO_2 and Co_3O_4, and no additional peaks were observed, indicating that no structural transformation or new phase formation occurred during synthesis.[41]

Morphological structure of SnO_2/Co_3O_4 nanoflowers.—The morphological structure of SnO_2/Co_3O_4 nanoflowers was analyzed using FE-SEM and STEM images, as illustrated in Figs. 2 and 3. Figure 2 depicts a nano-sized spherical flower-like structure with a rough surface, indicating a higher volume-to-surface ratio and consequently a greater surface area. Furthermore, the STEM images in Fig. 3 provide confirmation of the nano-sized form. Although the overall flower-like assemblies observed in FE-SEM exceed 100 nm, the STEM image (Fig. 3) reveals that these structures consist of thin nanosheets and nanograins. The mean crystallite size, calculated from the XRD peaks using the Scherrer Equation ($K = 0.9$, $\lambda = 1.5406$ Å), was approximately 21 nm (apparent), confirming that the primary crystalline domains are within the nanoscale range (Microchemical Journal, 208 (2025) 112 578).

Additional FE-SEM and STEM micrographs recorded from different regions are presented in the Supporting Information (Fig. S2–S3), confirming that the flower-like morphology and nanosheet features are consistent throughout the sample, with typical sheet widths below 100 nm.

The morphological superiority of the sensor is derived from its hierarchical nanoflower architecture. As evidenced by FE-SEM, these assemblies provide a high effective surface area; however, the true analytical advantage lies in their substructure. STEM analysis reveals that these "flowers" are meticulously composed of interconnected thin nanosheets and nanograins with widths strictly below 100 nm. This hierarchical arrangement prevents the aggregation of active sites and ensures that the entire SnO_2/Co_3O_4 surface is accessible for GIL interaction. By transitioning from a simple composite to a sophisticated "nanosheet-based" hierarchical framework, the modified CPE achieves a greater density of electroactive sites, leading to a marked improvement in current response compared to conventional electrode modifications.

The elemental composition of the composite was confirmed by EDX analysis (Fig. 4). The spectrum shows the characteristic O Kα (0.52 keV), Sn L-series (3.4–3.9 keV) and Co Kα/Kβ (6.93 and 7.65 keV) emission lines, with no signals of residual precursor or impurities, verifying the simultaneous presence of Sn, Co and O within the same region and thus the successful formation of the SnO_2/Co_3O_4 composite.

Electrochemical behavior study of the SnO_2/Co_3O_4/CPE.—In the present study, EIS and CV were applied to examine the electrode surfaces, employing KCl (0.1 M) and 5 mM ferricyanide solution. CV, performed by sweeping the potential cyclically while monitoring the resulting current, is a powerful approach to explore the redox activity of electroactive species. The resulting voltammograms offer

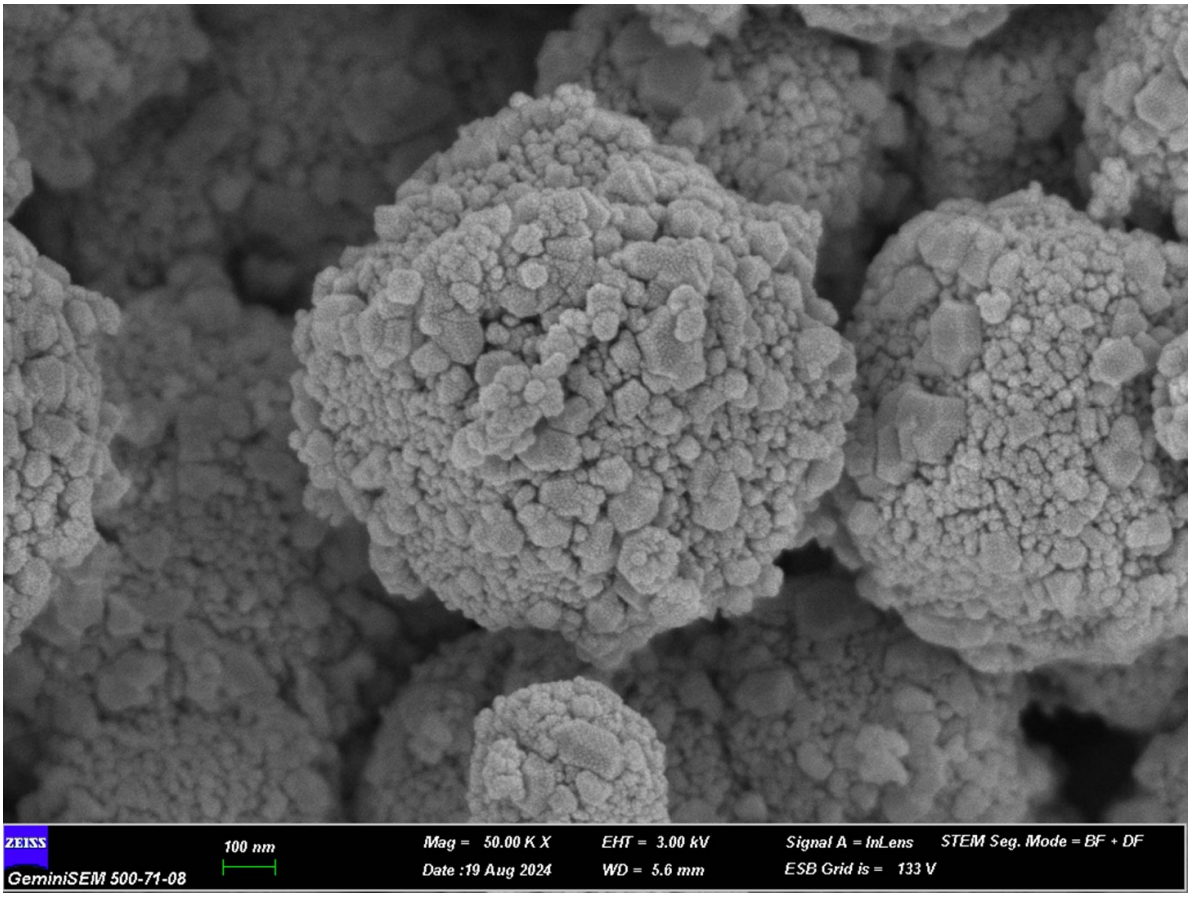


Figure 2. FE-SEM image of the SnO_2/Co_3O_4 hierarchical flower-like assemblies. The overall structures exceed 100 nm but are composed of nanoscale crystallites.

insights into surface properties, electrode coverage, and underlying reaction pathways.

Electrode systems, namely CPE and SnO_2/Co_3O_4/CPE, were examined through CV and EIS, as depicted in Figs. 5 A and B.

The cyclic voltammogram of the unmodified CPE (Fig. 5 A, pink line) displayed relatively low redox peak currents and a peak-to-peak separation (ΔE_p) of 0.37 V for hexacyanoferrate. Upon modification with SnO_2/Co_3O_4 (Fig. 5 A, green line), a notable enhancement in current response was observed, while maintaining the same ΔE_p value. This suggests that the incorporation of SnO_2/Co_3O_4 significantly improves electron transfer kinetics and increases the effective surface area. Therefore, the SnO_2/Co_3O_4/CPE was selected for further electrochemical studies.

The CV data on the electrochemical surface area of the electrodes were presented in Fig. S4. Calculations based on the Randles–Ševčík Equation (eq. S1) revealed an electrochemically active surface area (ECSA) of 0.091 cm^2 for the modified electrode, compared to 0.075 cm^2 for the bare CPE, as summarized in Table I. This increase reflects a greater density of electroactive sites, which enhances electron transfer and contributes to improved sensitivity and analytical performance.

EIS was employed to characterize the SnO_2/Co_3O_4-modified carbon paste electrode in a solution containing 5 mM ferricyanide and 0.1 M KCl. The electron transfer kinetics can be evaluated using the charge transfer resistance (R_{ct}), which corresponds to the diameter of the Nyquist semicircle.[42] As depicted in Fig. 5 B, the R_{ct} of the unmodified CPE was measured as 4300 Ω. Following successive modification with SnO_2/Co_3O_4, R_{ct} decreased to 2590 Ω, reflecting enhanced electron transfer at the electrode interface. The remarkable enhancement in the electrochemical response at the Sn_2/Co_3O_4/CPE can be attributed to the synergistic electrocatalytic effect arising from the intrinsic properties of the individual oxides and their unique interfacial interactions. Specifically, the contact between n-type SnO_2 and p-type Co_3O_4 leads to the formation of a p–n heterojunction at the nanostructured interface. This junction creates an internal electric field that significantly accelerates charge separation and facilitates the rapid migration of electrons toward the electrode surface. By effectively lowering the charge-transfer resistance, the SnO_2/Co_3O_4 composite acts as an efficient "electron bridge," bypassing the kinetic barriers typically observed at bare carbon surfaces. This accelerated interfacial electron transfer is fundamental to the diffusion-controlled electro-oxidation of GIL, ensuring a sharp, well-defined, and highly sensitive analytical signal. Collectively, the EIS results confirm the successful fabrication of the SnO_2/Co_3O_4/CPE.

From the EIS data and using eq. S2, the heterogeneous electron transfer rate constant (k^0) was calculated, providing a quantitative measure of the electron transfer kinetics at the electrode surface. The obtained k_0 values were evaluated as 0.62×10^{-4} cm s^{-1} for the unmodified GCE and 1.08×10^{-4} cm s^{-1} for the SnO_2/Co_3O_4/CPE, highlighting the superior charge transfer capabilities of the modified electrode (Table I).

Additionally, eq. S3 was applied to calculate the standard exchange current density (j_0). Standard exchange current density characterizes the rate of electron transfer when the system is at equilibrium. The bare CPE exhibited a j_0 of 0.059×10^{-4} A cm^{-2}, whereas the SnO_2/Co_3O_4/CPE demonstrated a significantly higher j_0 of 0.091×10^{-4} A cm^{-2}, indicating enhanced electrocatalytic activity due to the incorporation of the composite material (Table II).

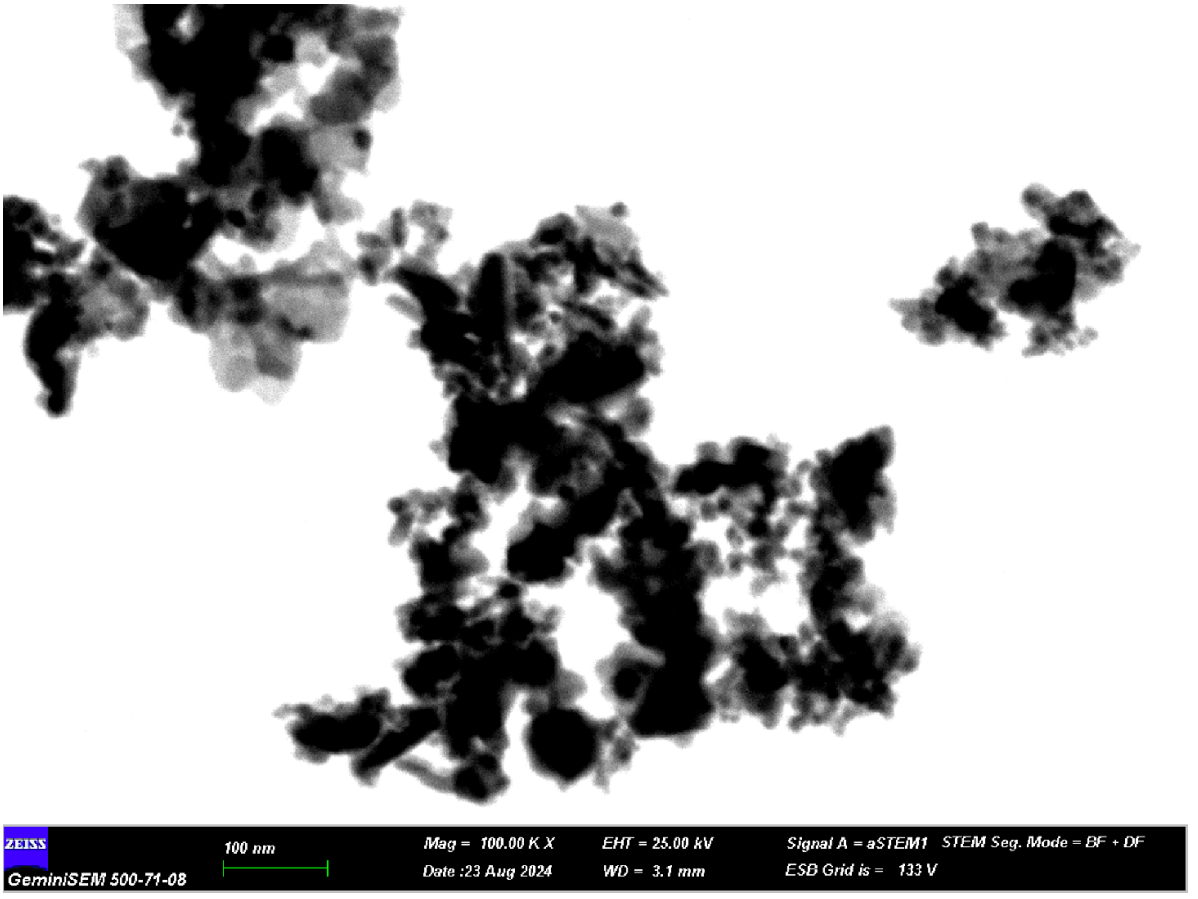


Figure 3. STEM image of SnO_2/Co_3O_4 showing nanosheet-and grain-like substructures (sub-100 nm features). Scale bar: 100 nm.

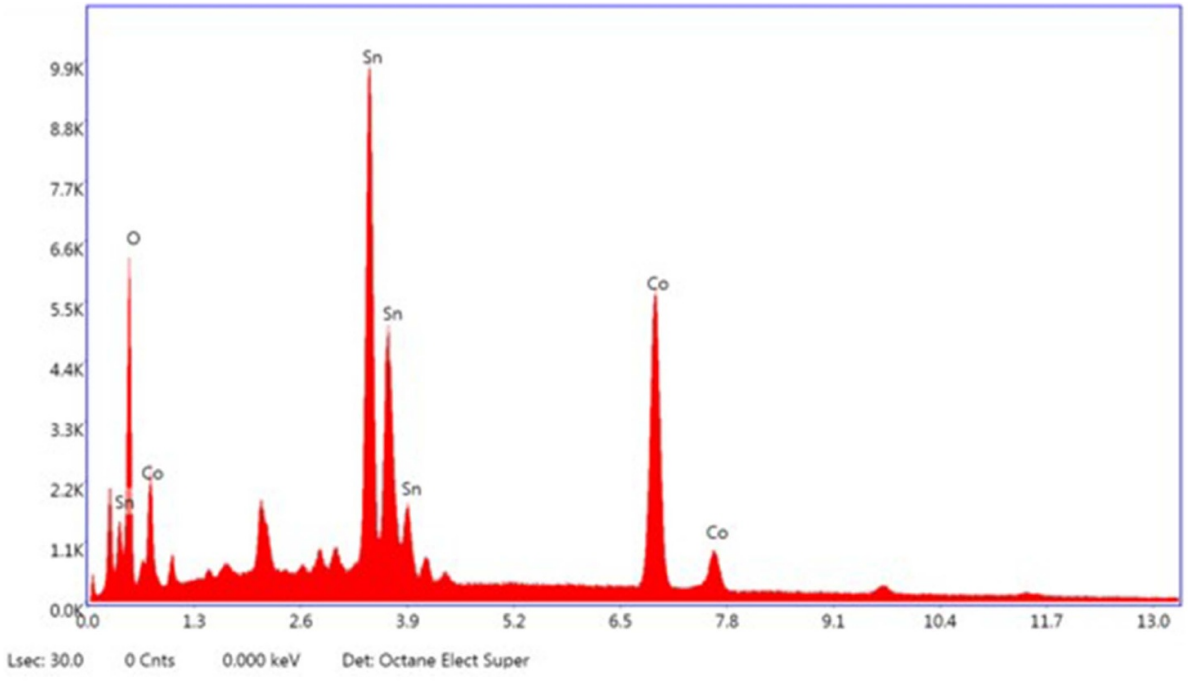


Figure 4. EDX spectrum of the SnO_2/Co_3O_4 nanoflowers, showing the characteristic emission lines of Sn, Co and O.

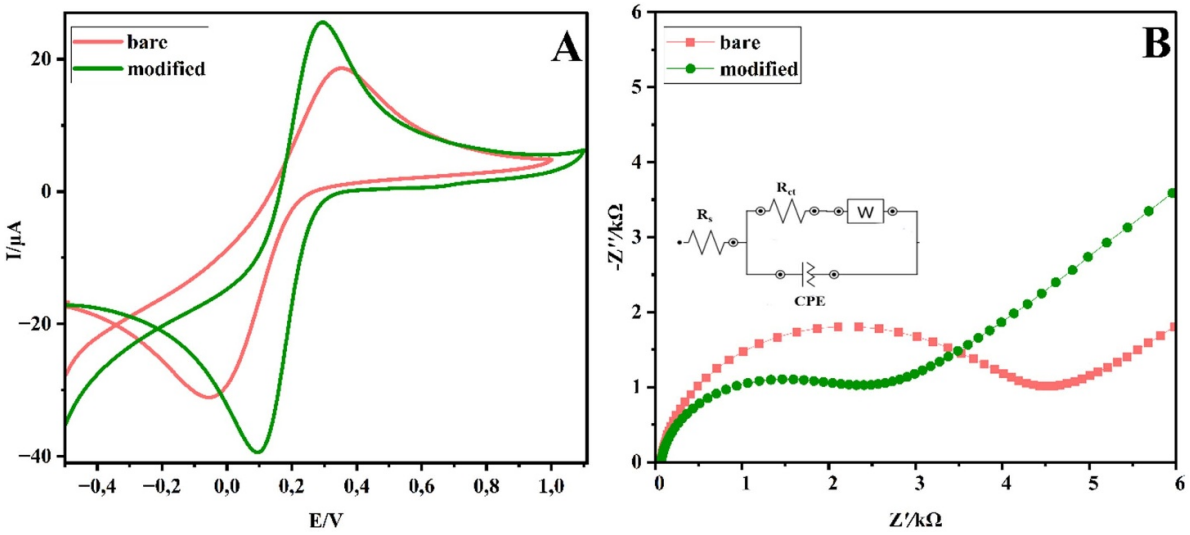


Figure 5. Cyclic voltammograms (A) and EIS spectras (B) of the bare electrode and SnO_2/Co_3O_4/CPE in 5 mM $[Fe(CN)_6]^{3-/4-}$ with KCl solution. The inset is the equivalent circuit for the EIS test of SnO_2/Co_3O_4/CPE (R_s: Electrolyte solution resistance, R_{ct}: Element of interfacial electron transfer resistance, CP: Constant phase element, W: Warburg impedance resulting from the diffusion of ions).

Table I. CV and EIS analysis of electrochemical behavior across electrode types.

Electrode	ΔE_p (V)	ECSA (cm^2)	k^0 (cm s^{-1})	j_0 (A cm^{-2})
Unmodified CPE	0.37	0.075	0.62×10^{-4}	0.059×10^{-4}
SnO_2/Co_3O_4/CPE	0.19	0.091	1.08×10^{-4}	0.091×10^{-4}

Investigation of GIL by voltammetry at the SnO_2/Co_3O_4/CPE.— GIL was examined using both CV (Fig. S5A) and DPV (Fig. S5B) at a bare CPE and a SnO_2/Co_3O_4-modified CPE. No significant current was observed in the absence of GIL, confirming minimal background interference. Upon addition of 50 μM GIL, the bare CPE showed a modest anodic response, while the modified electrode exhibited a substantially higher peak, reflecting enhanced electrocatalytic activity. DPV further revealed that the modified CPE produced a markedly stronger signal than the bare electrode, underscoring its improved sensitivity. Based on these results, quantitative analysis of GIL was carried out using DPV as the preferred voltammetric approach.

Experimental.—*Selection of the optimal supporting electrolyte.*—Various buffer systems (listed below, Fig. S6) were evaluated for the electrochemical detection of 50 μM GIL to determine the optimal supporting buffer solution. According to the DPV measurements, the PBS buffer solution provided the most intense and well-resolved oxidation peak, a result attributable to its wide buffering range and favorable pH that promote proton-assisted electron transfer. Thus, the PBS buffer solution was chosen as the supporting buffer in the electrochemical determination of GIL. Comparative outcomes are summarized in Fig. S6.

Effect of pH on GIL electrooxidation.—The influence of solution pH on the oxidation peak potential and current of 50 μM GIL was investigated using SnO_2/Co_3O_4/CPE in PBS over a pH range of 2.0–9.0 (Fig. S7A), given its critical effect on analyte stability and electrochemical behavior.[43]

The experimental results clearly demonstrate that the electrochemical response of GIL is strongly influenced by the pH of the medium. Both the peak potential (E_{pa}) and the corresponding peak current vary greatly with changes in pH, highlighting the crucial role of proton concentration in the redox process. As shown in the enlarged view (Fig. S7B), the highest oxidation peak current was obtained at pH 6.0; therefore, this pH was selected as the optimum condition for all subsequent electrochemical measurements. As illustrated in Fig. S7C, a gradual negative shift in E_{pa} was observed with increasing pH, and this behavior follows a well-defined linear relationship with an excellent coefficient of determination ($R^2 = 0.994$). The slope of this line, calculated as −39 mV per pH unit, is nearly half of the theoretical Nernstian value (−59 mV/pH). Such a deviation strongly suggests that the electron transfer mechanism involves the participation of two electrons coupled with the transfer of a single proton during the electrooxidation of GIL.

During the pH-dependent study, two oxidation peaks were observed at certain pH values, which is consistent with the existence of multiple electroactive sites in the GIL structure. In line with previous literature,[44] the peak displaying higher current intensity and superior definition was selected for further quantitative evaluation, as it ensured higher sensitivity and reproducibility of the measurements.

Peak current also varied with pH, rising steadily up to pH 6.0, where it slightly exceeded the value at pH 5.0, and then gradually decreasing at higher pH. Based on these observations, pH 6.0 was chosen as the optimal condition for subsequent electrochemical measurements.

Evaluation of scan rate effects.—The influence of the scan rate (ν) on the electrochemical oxidation of GIL (5 μM) at the SnO_2/Co_3O_4/CPE was systematically explored in PBS buffer (pH 6.0) across a wide potential sweep range of 10–300 mV s^{-1}. The cyclic voltammograms displayed a gradual positive displacement of the anodic peak potential as the scan rate increased, a feature that is characteristic of an irreversible electrochemical process. Although faint cathodic signals were seen on the reverse scan, they were not sufficiently well-defined for reliable quantitative application (Fig. S8A).[45]

When the anodic peak current was plotted against the square root of the scan rate, a strong linear correlation was obtained, expressed by the regression Equation $I_{pa} = 0.302\ \nu^{1/2} - 0.544$ ($R^2 = 0.995$).

Table II. Comparison of the electrochemical methods developed for the GIL quantification.

Analytical method	Linear range (μM)	LOD (μM)	LOQ/LLOQ (μM)	Application	Ref
HPLC	0.025–2.5	—	0.01	Human plasma	[11]
UPLC-MS/MS	0.001–0.5	—	0.001	Rats.	[13]
UPLC–ESI–MS/MS	0.001–3.0	0.00031	0.00095	Human liver microsomes.	[12]
DPV (NiCaCr-LTH@Nb_2C MXene/GCE)	0.005–11.640	0.001	0.003	Human urine, human plasma and tablets.	[15]
DPV (SnO_2/Co_3O_4/CPE)	0.00031–11.640	0.000093	0.000309	Human urine, human plasma and tablets.	This study.

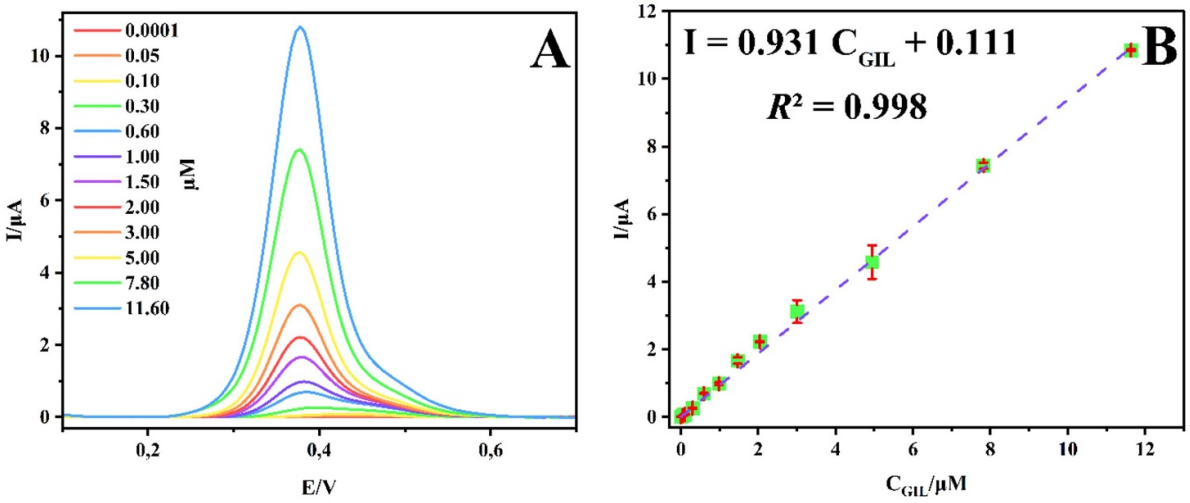


Figure 6. (A) Differential pulse voltammograms of the SnO_2/Co_3O_4/CPE at increasing GIL levels, and (B) the related calibration graph plotting I (μA) against concentration of GIL (μM).

This behavior indicates that the overall charge-transfer process is predominantly controlled by diffusion rather than surface adsorption of the analyte (Fig. S8B).[45] Additional evidence supporting this interpretation was provided by the log–log analysis, where the plot of log I_{pa} versus log ν yielded a straight line (log I_{pa} = 0.615 log ν−0.847, R^2 = 0.999) with a slope very close to the theoretical value of 0.5 expected for a diffusion-driven mechanism (Fig. S8C).[46]

Moreover, examination of the anodic potential as a function of the natural logarithm of the scan rate produced a linear dependence described by E_{pa} = 0.013 ln ν + 0.361 (R^2 = 0.994, Fig. S8D). Interpretation of this relationship using Laviron's theoretical framework for irreversible electrode processes (eq. S4) allowed the electron number participating in the process to be estimated at approximately two. Taken together with the earlier pH-dependence study, which implied the participation of a single proton, the results strongly suggest that the electrooxidation of GIL progresses through a 2-electron, 1-proton transfer mechanism.

Analytical performance evaluation of GIL by DPV.—Under optimized conditions, the quantification of the target analyte (GIL) was performed using the SnO_2/Co_3O_4/CPE coupled with the DPV technique. The voltammograms recorded at varying GIL concentrations, along with the corresponding calibration curve, are presented in Figs. 6(A) and (B), respectively. The observed anodic peak currents increased proportionally with GIL concentration over the range of 0.00031–11.60 μM. Within this wide linear range, no signs of surface saturation or fouling were observed, even at the upper concentration levels. This behavior is attributed to the highly diffusive nature of GIL oxidation, as confirmed by the scan-rate studies, and to the renewable microstructure of the carbon paste matrix, which minimizes surface blockage. Additionally, the SnO_2/Co_3O_4 composite provides a high surface area and low charge-transfer resistance, facilitating efficient mass transport and preventing peak distortion at elevated analyte concentrations.

In this concentration interval, the calibration curve followed a linear regression model defined by the Equation I_{pa} (μA) = 0.931C_{GIL} + 0.111, exhibiting an excellent coefficient of determination (R^2 = 0.998). LOD and LOQ were calculated to be 0.000093 μM and 0.000309 μM, respectively, based on the IUPAC-recommended approach (LOD = 3Sb/m, LOQ = 10Sb/m), where Sb denotes the standard deviation of the blank and m represents the slope of the calibration curve. The sensitivity of the sensor was calculated as the slope of the calibration curve divided by the surface area of the working electrode (diameter = 3.00 mm), resulting in a value of 13.17 μA μM^{-1} cm^{-2}. This value indicates a high response per unit concentration and per unit area, reflecting excellent analytical performance. Detailed analytical performance data of the developed method are summarized in Table S1.

To further contextualize the analytical performance of the proposed SnO_2/Co_3O_4/CPE sensor, a comparison with previously reported methods for the quantification of GIL is provided in Table II. The table summarizes the linear ranges, limits of detection/quantification, electrode materials (where applicable), and application matrices for various analytical platforms, including chromatographic and electrochemical techniques. As shown, the present SnO_2/Co_3O_4/CPE-based method offers a broader linear range and lower LOD/LOQ values compared to other approaches, while maintaining successful applicability in spiked samples and tablet formulation. This highlights the advantage of the developed electrode material and underscores its suitability for practical bioanalytical applications.

Assessment of sensor repeatability and reproducibility.—Repeatability is an important parameter for evaluating the reliability of an electrochemical sensor. In order to investigate the repeatability of the proposed SnO_2/Co_3O_4/CPE sensor, ten consecutive DPV measurements were carried out using a 5 μM GIL solution under the same experimental conditions. The results indicated excellent repeatability, with a relative standard deviation (RSD) of 1.1% obtained from the repeated measurements (Fig. S9). The low RSD value highlights the high precision and operational stability of the sensor, demonstrating its ability to provide consistent and reliable electrochemical signals.

Furthermore, the reproducibility of the sensor was examined to verify the uniformity of sensor performance across independently prepared electrodes. To this end, nine SnO_2/Co_3O_4/CPE electrodes were fabricated under the same conditions, and DPV responses were recorded for 5 μM GIL (Fig. S10). The resulting RSD was 0.5%, demonstrating excellent reproducibility and indicating the robustness of the sensor fabrication process. These outcomes affirm the sensor's suitability for practical applications, offering both precision and consistency in electrochemical measurements.

Analytical selectivity and interference study of SnO_2/Co_3O_4/CPE.—The ability of the SnO_2/Co_3O_4/CPE sensor to selectively detect GIL in the presence of potential interferents was carefully examined by utilizing DPV. Experiments were conducted with 5 μM GIL solutions supplemented with a range of biologically and pharmaceutically relevant compounds. The selected

Table III. Analytical performance of the SnO_2/Co_3O_4/CPE sensor for GIL determination in spiked biological and pharmaceutical samples.

Sample	Initial (μM)	Added (μM).	Found (μM).	RSD (%)	Recovery (%).
Human urine.	—	2.0	2.01	0.3	100.58
		3.0	3.03	0.4	101.25
		5.0	5.02	0.7	100.41
Human plasma	—	2.0	1.96	0.1	96.86
		3.0	3.1	1.4	103.46
		5.0	4.85	1.2	97.05
Tablet	2.0	0	2.05	1.2	102.69
	3.0	0	2.98	1.2	99.37
	5.0	0	4.92	1.2	98.50

interferents (listed below, Fig. S11) included species with structural resemblance to GIL, compounds commonly present in biological fluids, and molecules with known electroactivity that might overlap with the target signal.

The voltammetric profiles obtained under optimized conditions revealed that none of these coexisting species produced a noticeable alteration in the GIL oxidation peak. This outcome provides clear evidence of the strong selectivity of the proposed sensor (Fig. S11A). Furthermore, the RSD of the measured peak currents in the presence of all tested interferents was as low as 0.38%, reflecting minimal variability and confirming the excellent reproducibility of the sensor response. Taken together, the absence of significant interference even in the presence of structurally related drugs at a 2-fold excess and other potential interferents at a 20-fold excess demonstrates the high selectivity of the proposed sensor in complex real-world matrices, including biological samples and pharmaceutical formulations.

Real-world utilization of the SnO_2/Co_3O_4/CPE.—The real-world utility of the SnO_2/Co_3O_4/CPE sensor was assessed through its application to human plasma, urine samples, and commercial tablet formulations. To rigorously evaluate the sensor's selectivity and tolerance to matrix effects independent of extraction variability, recovery experiments were conducted by spiking the analyte into the processed biological matrices (i.e. after protein precipitation or filtration). In pharmaceutical analysis, since the tablet formulation already contains the active compound, the recovery was calculated based on the known content of the active ingredient. DPV carried out under optimized conditions provided recovery values in the range of 96.86%–103.46%, while the corresponding relative standard deviations remained consistently below 1.41%. To statistically confirm the reliability of these results, Student's *t*-tests were performed following the approach described in recent literature.[47] The calculated t_{exp} values for all samples were lower than the critical *t* value (4.303, $n = 3$, 95% confidence level), indicating no significant difference between the measured and theoretical concentrations. These findings reflect the high accuracy, precision, and consistency of the proposed method within these complex ionic and organic environments. Collectively, the results validate the robustness of the sensor for quantitative determination of GIL in complex biological fluids and pharmaceutical preparations. A detailed overview of the recovery is presented in Table III, while the full *t*-test data, calculations and *t*-test results are provided in Table S2.

Stability.—The long-term storage stability of the SnO_2/Co_3O_4/CPE was also evaluated to assess its potential for routine analytical applications. The modified electrode was stored at room temperature when not in use, and its electrochemical response to 5.0 μM GIL was monitored intermittently over a period of 10 d, as illustrated in Fig. S12. The sensor displayed remarkable stability, with the oxidation peak current decreasing only slightly from 5.30 μA (Day 1) to 5.04 μA (Day 10). This corresponds to a signal retention of 95.1%, demonstrating that the SnO_2/Co_3O_4 nanocomposite effectively preserves the active surface sites and prevents significant sensor degradation over time.

Greenness and sustainability assessment.—The environmental sustainability of the proposed electrochemical approach was evaluated using the Greenness Evaluation Metric for Analytical Methods (GEMAM), which is based on the core principles of Green Chemistry. This assessment framework examines various stages of the analytical process, such as sample preparation and storage, the type and amount of reagents used, analytical performance and method features, instrumentation requirements, waste production, and impacts related to the analyst.[48] The resulting GEMAM pictogram (Fig. S13) confirms that the developed voltammetric method exhibits a high level of environmental compatibility, showing particularly favorable results in terms of reagent usage, instrumental demands, waste minimization, and operator safety.

The strong green profile of the proposed method mainly stems from its straightforward sample preparation, which consists solely of dissolving the analyte in a minimal amount of ethanol followed by dilution with an aqueous buffer. This procedure eliminates the need for derivatization, extraction, or energy-demanding pretreatment steps. The use of environmentally friendly solvents, namely ethanol and water, along with the small total solution volume required for each analysis (10 ml), markedly decreases both reagent consumption and waste production. In addition, the potentiometric technique operates with very low energy requirements and relies on compact, reusable instrumentation, further enhancing its environmental sustainability. High operator safety is also ensured, as the method avoids the use of toxic chemicals, elevated pressures, extreme temperatures, or radiation sources.

Although the GEMAM evaluation reveals a comparatively higher score associated with the sample-related criterion, this outcome is primarily linked to the ex-situ sample preparation approach, which represents practical laboratory conditions rather than added methodological complexity. Importantly, this factor does not detract from the overall environmental merits of the method. The final GEMAM score of 5.96 clearly demonstrates that the proposed SnO_2/Co_3O_4-based potentiometric sensor offers a green, economical, and sustainable analytical option for the determination of GIL in pharmaceutical and biological matrices, providing distinct advantages over more resource-intensive chromatographic methods.

DFT studies of GIL.—The geometry of the GIL molecule was optimized using density functional theory (DFT) at the B3LYP/6–31 + G(d,p) level to determine its total energy, frontier orbital characteristics, and key quantum chemical descriptors. The optimized 3D

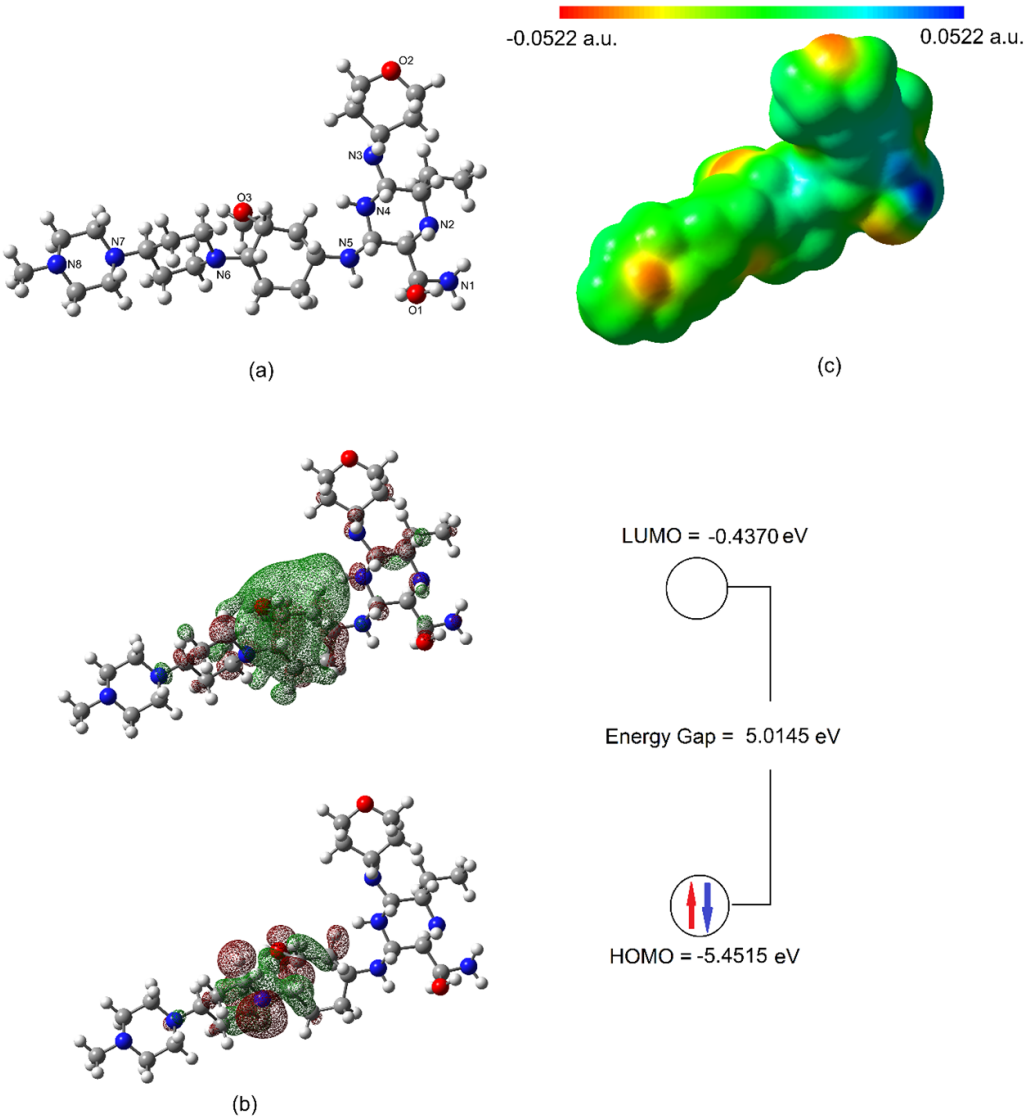


Figure 7. (a) Optimized geometry (b) electron densities surface and energy values of HOMO and LUMO of (GIL) (c) MEP surfaces.

structure together with the HOMO–LUMO and molecular electrostatic potential (MEP) surfaces are presented in Fig. 7, while the calculated reactivity parameters are summarized in Table S3.

Frontier molecular orbitals play a crucial role in determining the electronic properties and chemical reactivity of molecules. The HOMO and LUMO energies represent the electron-donating and electron-accepting abilities of a compound, respectively. The HOMO–LUMO energy gap (ΔE_{Gap}) provides insight into the molecule's stability and reactivity.[37] The optimized GIL molecule was analyzed to obtain its total energy, frontier orbital energies, and electronic configurations. For GIL, ΔE_{Gap} was calculated as 5.0145 eV, indicating moderate electronic reactivity. As shown in Fig. 7(b), both orbitals exhibit π-type character. The HOMO density is mainly localized on the methoxyphenyl and N-methyl pyrazine-2-carboxamide moieties, while the LUMO distribution is primarily observed over the methoxyphenyl and pyridine rings. Based on the orbital energies, several quantum chemical descriptors including ionization potential (IP), electron affinity (EA), chemical hardness (η), electronegativity (χ), and softness (σ) were calculated using Koopmans' theorem,[36] and the results are summarized in Table S3.

Molecular electrostatic potential (MEP) mapping was also carried out to visualize the charge distribution and predict potential reactive regions of GIL. The color-coded MEP map illustrates electrostatic potential variations across the molecular surface, where red regions indicate electron-rich (electrophilic attack) zones, blue regions denote electron-deficient (nucleophilic attack) sites, and green areas correspond to neutral potential regions.[49] The MEP surface Fig. 7(c) shows electron-rich regions mainly localized on oxygen and nitrogen atoms, whereas positive potential regions are associated with hydrogen atoms of the carboxamide group. These regions represent possible sites for electrophilic and nucleophilic interactions and may contribute to intermolecular hydrogen bonding during molecular docking analysis. The computational findings provide a robust molecular-level justification for the experimental voltammetric behavior of GIL. The calculated HOMO energy level (−5.4515 eV) and the relatively moderate ΔE_{Gap} (5.0145 eV) align perfectly with the observed oxidation potential at the SnO_2/Co_3O_4/CPE, indicating a molecule that is electrochemically active yet stable. The spatial distribution of the HOMO density, predominantly localized on the methoxyphenyl and N-methyl pyrazine-2-carboxamide moieties, identifies these as the primary

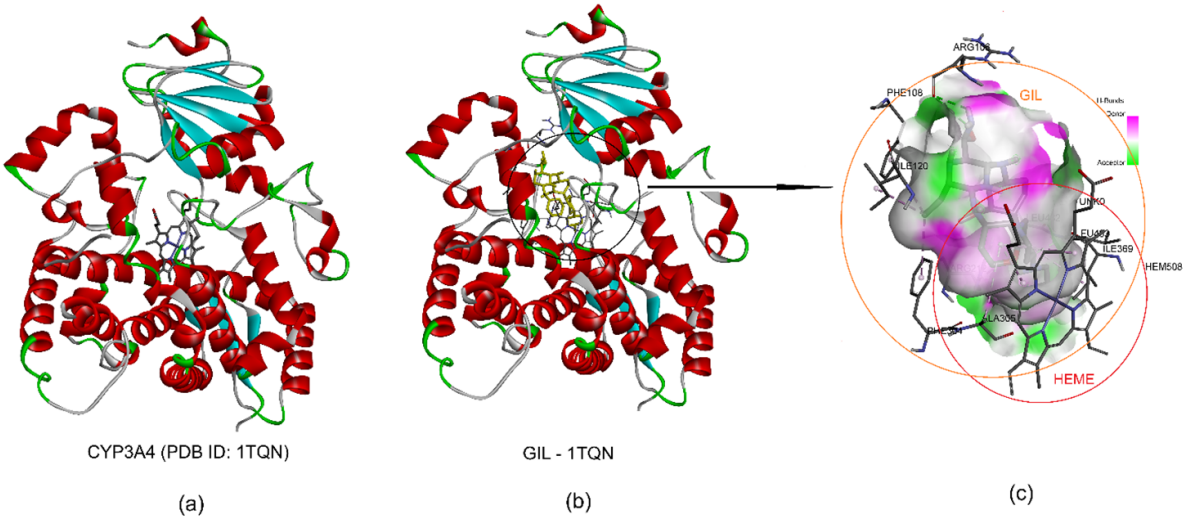


Figure 8. (a) Structure of the cytochrome P450 enzyme CYP3A4 (PDB ID: 1TQN); (b) the lowest-energy binding configuration of CYP3A4 with GIL (shown in yellow); (c) visualization of the hydrogen-bonding surface and spatial proximity of the GIL ligand to the heme group in the lowest-energy docked complex.

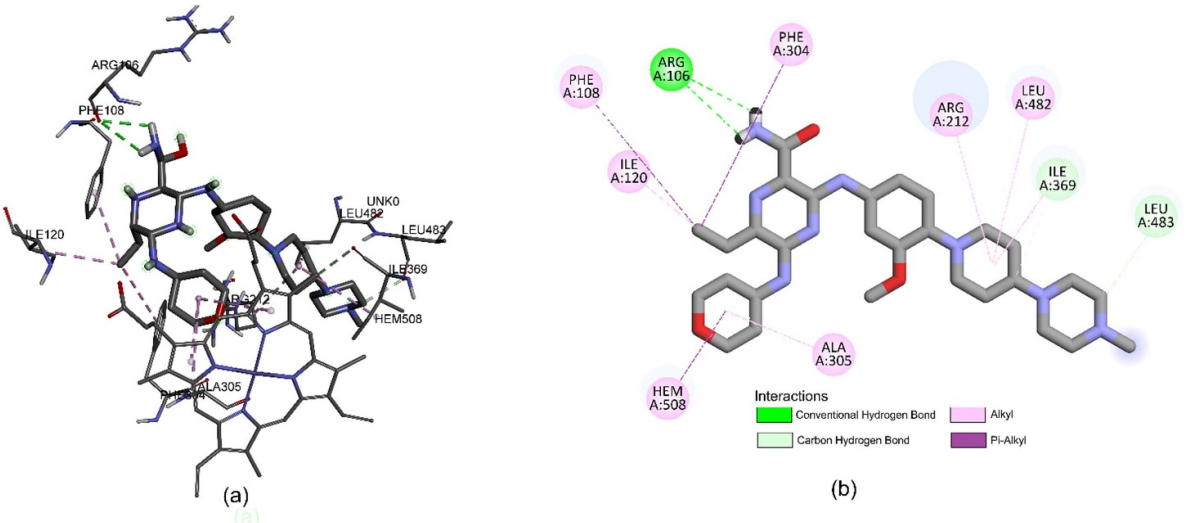


Figure 9. (a) 3D The non-covalent interactions at most favorable docked poses, (b) 2D interaction graph of the compound GIL in the catalytic pockets of the cytochrome P450 enzyme CYP3A4 (PDB ID: 1TQN).

sites of electron abstraction. This theoretical localization directly supports the experimentally derived $2e^{-}/1\ H^{+}$ mechanism, suggesting that the initial electron transfer occurs at these electron-rich regions, followed by rapid deprotonation to form the stable iminium intermediate. Furthermore, the MEP mapping confirms that the high electron density at these sites makes them highly susceptible to the electrocatalytic environment provided by the SnO_2/Co_3O_4 nanoflowers, resulting in the exceptionally low detection limits achieved in this study. Overall, the DFT calculations provide a molecular-level explanation for the electrochemical behavior of GIL (Scheme S1).

Molecular docking studies.—Although GIL is generally well tolerated, clinical studies have reported several treatment-related adverse events, including anemia, febrile neutropenia, and thrombocytopenia.[9,10] Because GIL undergoes hepatic metabolism primarily via the cytochrome P450 enzyme CYP3A4, monitoring its interactions with this enzyme is important for understanding potential drug–drug interactions and pharmacokinetic behavior.

Molecular docking simulations were therefore performed to investigate the interaction between the optimized GIL molecule and the catalytic pocket of CYP3A4 (PDB ID: 1TQN). The calculated binding energies and RMSD values are summarized in Table S4. The most stable docking conformation exhibited a binding energy of -7.4 kcal mol^{-1}. The docked structure of GIL within the active site of CYP3A4 together with the heme cofactor is presented in Fig. 8, while the detailed interaction profiles are summarized in Table S5 and illustrated in Fig. 9.

The docking analysis revealed that GIL interacts with several amino acid residues within the catalytic pocket, including ARG106, PHE304, PHE108, ILE120, ALA305, ARG212, ILE369, LEU482, and LEU483. Two conventional hydrogen bonds were formed between the hydrogen atoms (H1 and H2) of the N1 atom in the carboxamide group of GIL and the oxygen atom of ARG106, with bond lengths of 2.7088 and 2.8811 Å. These interactions indicate that the carboxamide moiety represents an important region for molecular recognition and charge transfer.

In addition, GIL interacts with the heme cofactor (HEM508) through two π–alkyl interactions with distances of 4.3388 and 4.7763 Å. Additional stabilizing interactions, including π–alkyl, alkyl, and carbon–hydrogen contacts, were also observed between GIL and surrounding amino acid residues. These non-covalent interactions contribute to the stability of the GIL–CYP3A4 complex.

The docking results are consistent with the molecular electrostatic potential (MEP) analysis, which identified the hydrogen atoms of the N1 carboxamide group as potential reactive sites for intermolecular interactions. Overall, the docking analysis provides molecular-level insight into the interaction of GIL with CYP3A4 and supports the experimentally observed charge-transfer behavior relevant to its electrochemical response.

Conclusions

In conclusion, a novel, sensitive, and eco-friendly electrochemical sensor based on a SnO_2/Co_3O_4-modified carbon paste electrode was successfully developed for the determination of GIL. Method validation was systematically performed in strict compliance with ICH Q2(R1) guidelines and IUPAC recommendations, demonstrating excellent analytical performance, including high sensitivity, a linear range, a low detection limit, and outstanding selectivity. The electro-oxidation mechanism of GIL was elucidated through pH-dependent and scan-rate studies supported by density functional theory (DFT) calculations. The observed pH slope (−39 mV/pH) suggested a $2e^-/1\ H^+$ transfer process, while HOMO localization indicated the methoxyphenyl and N-methyl pyrazine-2-carboxamide groups as the main oxidation sites, supporting a mechanism involving electron transfer followed by deprotonation and iminium cation formation.

The applicability of the proposed method was confirmed by successful determination of GIL in pharmaceutical formulations and biological matrices, including human plasma and urine. Green analytical chemistry assessments (GEMAM) further demonstrated the environmental compatibility of the method. In addition, DFT and molecular docking studies revealed key electronic properties of GIL and its interaction with the CYP3A4 enzyme through hydrogen bonding with ARG106 and π-alkyl interactions with the heme group. These findings provide insight into the molecular basis of GIL reactivity and its potential metabolic interactions. Overall, the proposed sensor offers a simple, reliable, and sustainable platform for the determination of GIL in pharmaceutical and biological samples.

Acknowledgments

DFT calculations reported in this study were partially performed at ULAKBIM/TRUBA (TUBITAK). This work was supported by the BAP Unit of Ankara University (A.U. BAP) under Project No. TSA-2025-3852. The author Ç. A. Özata is supported by the Scientific and Technological Research Council of Turkey (TÜBİTAK) under the 2211–A National PhD Scholarship Program.

Data availability statement

The data supporting the findings of this study are available within the article and its Supplementary Information files. Additional data related to this study may be available from the corresponding author upon reasonable request.

Funding Declaration

This research did not receive any specific grant from funding agencies in the public, commercial, or not-for-profit sectors.

Ethics approval

No approval of research ethics committees was required to accomplish the goals of this study because synthetic materials were used in the experimental study.

ORCID

Çiğdem Aybüke Özata https://orcid.org/0009-0003-8281-2108
Nevin Erk https://orcid.org/0000-0001-5366-9275
Celal Tuğrul Zeyrek https://orcid.org/0000-0001-6744-7841
Furkan Uzcan https://orcid.org/0000-0001-6831-3087
Mustafa Soylak https://orcid.org/0000-0002-1017-0244

References

1. A. Redner and R. Kessel, *Lanzkowsky's Man. Pediatr. Hematol. Oncol.*, 439 (**2022**).
2. I. Olsson, G. Bergh, M. Ehinger, and U. Gullberg, *Eur. J. Haematol.*, **57**, 1 (1996).
3. E. Patkowska, A. Szczepaniak, M. Barańska, M. Kaźmierczak, M. Paluszewska, W. Jędrzejczak, R. Guzicka-Kazimierczak, W. Knopińska-Posłuszny, O. Grzybowska-Izydorczyk, and A. Pluta, *J. Leuk*, **7**, 1 (2019).
4. W. N. Abd-alghafar, R. A. Shabana, R. El-Shaheny, and M. M. Tolba, *Microchem. J.*, **204**, 111078 (2024).
5. Z. Malekinejad, A. Baghbanzadeh, A. Nakhlband, B. Baradaran, S. Jafari, Y. Bagheri, F. Raei, S. Montazersaheb, and R. Farahzadi, *Life Sci.*, **306**, 120809 (2022).
6. S. Moharram, *Role of FLT3 in Acute Myeloid Leukemia: Molecular Mechanisms and Therapeutic Opportunities*, Lund University, (2021).
7. C. Kang, and H. A. Blair, *Target. Oncol.*, **15**, 681 (2020).
8. I. Konstantinidis, S. Tsokkou, S. Grigoriadis, L. Chrysavgi, and E. Gavriilaki, *Cancers*, **16**, 2474 (2024).
9. A. Solana-Altabella, J. E. Megías-Vericat, O. Ballesta-López, D. Martínez-Cuadrón, and P. Montesinos, *Expert Rev. Clin. Pharmacol.*, **16**, 133 (2023).
10. J. E. Megías-Vericat, A. Solana-Altabella, O. Ballesta-López, D. Martínez-Cuadrón, and P. Montesinos, *Ann. Hematol.*, **99**, 1989 (2020).
11. T. Yasu, T. Sugi, K. Momo, M. Hagihara, and H. Yasui, *Biomed. Chromatogr.*, **35**, e5028 (2021).
12. M. W. Attwa, H. AlRabiah, A. M. Alsibaee, A. S. Abdelhameed, and A. A. Kadi, *Separations*, **10**, 278 (2023).
13. Q. Wang, Z. Chen, D. Chen, and X. Y. Ye, *Dev. Ther.*, 2061 (2020).
14. B. Vuyyala, K. P. Pisini, and D. Swain, *Anal. Methods.*, **16**, 6856 (2024).
15. Ç. A. Özata, N. Erk, W. Bouali, A. A. Genc, H. E. H. Ahmed, and M. Soylak, *Electrochim. Acta*, **539**, 147089 (2025).
16. M. Chu, W. Tian, J. Zhao, M. Zou, Z. Lu, D. Zhang, and J. Jiang, *Chemosphere*, **307**, 136024 (2022).
17. Y. Li, R. Xu, H. Wang, W. Xu, L. Tian, J. Huang, C. Liang, and Y. Zhang, *Biosensors*, **12**, 377 (2022).
18. B. Yan, W. Liu, Y. Sun, M. Gao, A. Chen, and J. Zhang, *Mater.*, **18**, 1869 (2025).
19. P. Jiang, H. Zhang, C. Chen, J. Liang, Y. Luo, M. Zhang, and M. Cai, *CrystEngComm*, **19**, 5742 (2017).
20. J. Penagos-Llanos, O. García-Beltrán, J. Calderón, E. Nagles, and J. Hurtado, *Electroanalysis*, **31**, 695 (2019).
21. A. M. Attaran, S. Abdol-Manafi, M. Javanbakht, and M. Enhessari, *J. Nanostruct. Chem.*, **6**, 121 (2016).
22. G. Li, *J. Appl. Phys.*, **127** (2020).
23. B. Cen, K. Li, C. Lv, and R. Yang, *J. Solid State Electrochem.*, **24**, 687 (2020).
24. N. Hareesha, and J. Manjunatha, *J. Iran. Chem. Soc.*, **17**, 1507 (2020).
25. B. Chandrashekar, B. K. Swamy, M. Pandurangachar, S. S. Shankar, O. Gilbert, J. Manjunatha, and B. Sherigara, *Int. J. Electrochem. Sci.*, **5**, 578 (2010).
26. H. Beitollahi, S. Tajik, M. H. Asadi, and P. Biparva, *J. Anal. Sci. Technol.*, **5**, 29 (2014).
27. C. M. Kuskur, B. K. Swamy, and H. Jayadevappa, *Ionics*, **25**, 1845 (2019).
28. A. S. Saad, A. M. A. Al-Alamein, M. M. Galal, and H. E. Zaazaa, *J. Electrochem. Soc.*, **166**, B103 (2019).
29. M. Choukairi, L. Hejji, M. Achache, M. H. Touil, D. Bouchta, K. Draoui, and A. Azzouz, *Talanta*, **276**, 126247 (2024).
30. M. Achache, J. J. García-Guzmán, N. B. Seddik, L. Cubillana-Aguilera, J. M. Palacios-Santander, D. Bouchta, and M. Choukairi, *Diam. Relat. Mater.*, **154**, 112141 (2025).
31. A. D. Becke, *J. Chem. Phys.*, **98**, 5648 (1993).
32. A. M. Elasbali, A. E. M. Elayyan, S. H. Alharethi, T. Mohammad and M. I. Hassan, *Comput. Biol. Chem.*, 108636 (2025).
33. U. Das, L. Chandramouli, A. Uttarkar, J. Kumar, and V. Niranjan, *Asp. Mol. Med.*, **5**, 100058 (2025).
34. W. Li, F. Yang, B. Huang, Z. Liu, H. Meng, J. Zheng, B. Zeng, J. Yang, Y. Li, and S. Xiao, *Ionics*, **26**, 6125 (2020).
35. N. Erk, C. A. Ozata, W. Bouali, A. A. Genc, H. E. H. Ahmed, Q. Salamat and M. Soylak, *Ind. Eng. Chem. Res.*, **64**, 6240 (2025).
36. T. Koopmans, *Physica*, **1**, 104 (1933).
37. T. C. Zeyrek, *Korean Chemical Society*, **57**, 461 (2013).
38. A. Gurung, M. Ali, A. Bhattacharjee, M. AbulFarah, F. Al-Hemaid, F. Abou-Tarboush, K. Al-Anazi, F. Al-Anazi, and J. Lee, *Genet. Mol. Res.*, **15**, 1 (2016).
39. M. M. Rahman, S. B. Khan, M. Faisal, M. A. Rub, A. O. Al-Youbi, and A. M. Asiri, *Talanta*, **99**, 924 (2012).
40. S. Zhao, C. Li, J. Liu, N. Liu, S. Qiao, Y. Han, H. Huang, Y. Liu, and Z. Kang, *Carbon N. Y.*, **92**, 64 (2015).
41. P. Murugesh, M. Ganesan, P. S. Udaiyar, H. S. Krishnan, A. Jayaram, and N. Mani, *ACS Appl. Nano Mater.*, **6**, 17433 (2023).

42. M. Achache, D. Bouchta, K. Draoui, and M. Choukairi, *Inorg. Chem. Commun.*, **174**, 114120 (2025).
43. N. Hareesha, and J. Manjunatha, *J. Electroanal. Chem.*, **878**, 114533 (2020).
44. W. Bouali, N. Erk, A. A. Genc, Q. Salamat, and M. Soylak, *Microchem. J.*, **207**, 112058 (2024).
45. M. Achache, S. El-Haddar, H. E. Haddaoui, G. E. Idrissi, K. Draoui, D. Bouchta, and M. Choukairi, *Mater. Chem. Phys.*, **332**, 130313 (2025).
46. W. Bouali, A. A. Genc, N. Erk, G. Kaya, B. Sert, and K. Ocakoglu, *Microchim. Acta*, **191**, 135 (2024).
47. G. E. Idrissi, M. Achache, H. E. Haddaoui, S. El-Haddar, K. Draoui, D. Bouchta, and M. Choukairi, *J. Water Process Eng.*, **75**, 107928 (2025).
48. T. Xin, L. Yu, W. Zhang, Y. Guo, C. Wang, Z. Li, J. You, H. Xue, M. Shi, and L. Yin, *J. Pharm. Anal.*, **15**, 101202 (2025).
49. E. Scrocco, and J. Tomasi, *Adv. Quantum Chem*, Academic (1978).